

Oxygen-induced step bunching and faceting of Rh(553): Experiment and *ab initio* calculations

J. Gustafson, A. Resta, A. Mikkelsen, R. Westerström, J. N. Andersen, and E. Lundgren*
Department of Synchrotron Radiation Research, Lund University, Box 118, S-221 00 Lund, Sweden

J. Weissenrieder
MAX-lab, Lund University, Box 118, S-221 00 Lund, Sweden

M. Schmid and P. Varga
Institut für Allgemeine Physik, Technische Universität Wien, A-1040 Wien, Austria

N. Kasper
Max-Planck Institut für Metallforschung, Heisenbergstrasse 3, D-70569 Stuttgart, Germany

X. Torrelles
Institut de Ciencia de Materials de Barcelona (C.S.I.C.), 08193 Bellaterra, Barcelona, Spain

S. Ferrer
European Synchrotron Radiation Facility, Boîte Postale 220, 28043 Grenoble Cedex, France

F. Mittendorfer and G. Kresse
Institut für Materialphysik, Universität Wien, A-1090 Wien, Austria
 (Received 24 March 2006; revised manuscript received 19 May 2006; published 5 July 2006)

Using a combined experimental and theoretical approach, we show that the initial oxidation of a Rh(553) surface, a surface vicinal to (111), undergoes step bunching when exposed to oxygen, forming lower-index facets. At a pressure of about 10^{-6} mbar and a temperature of 380 °C this leads to (331) facets with one-dimensional oxide chains along the steps, coexisting with (111) facets. Further increase of the pressure and temperature results in (111) facets only, covered by an O-Rh-O surface oxide. Our density functional theory calculations provide an atomistic understanding of the observed behavior.

DOI: [10.1103/PhysRevB.74.035401](https://doi.org/10.1103/PhysRevB.74.035401)

PACS number(s): 68.35.Bs, 68.37.Ef, 68.43.Bc, 79.60.-i

I. INTRODUCTION

The search for a fundamental understanding of solid surfaces and their interaction with a surrounding gas has been a major research field for decades, motivated by areas such as, e.g., catalysis, corrosion, and thin-film devices. Using model systems such as low-index single-crystal surfaces under ultrahigh-vacuum (UHV) conditions and carefully controlling the reactant gas abundance on the surface, significant progress has been made in the understanding of adsorbate-adsorbate and adsorbate-substrate interactions.¹ A consequence of this surface science approach is the introduction of a pressure and a material gap by which surface properties and reactivity probed and determined under well-defined UHV conditions may not be extrapolated in a straightforward manner to those at realistic reaction conditions.²

Recently, a large effort has been made to extend these studies of the atomic-scale structure to systems of a complexity at least approaching that found in nature. Structural studies at atmospheric pressures using CO and H have been performed *in situ* using a number of well-prepared single-crystal substrates; see, for example, Refs. 3–5. Further, a growing number of studies have concentrated on the *in situ* oxidation and reactivity of late transition metals.^{6–13} Surprisingly, it has been shown that under realistic conditions, the resulting oxides are more active in CO oxidation than the metal surfaces.^{6,7,11,14} Studies of late transition-metal sur-

faces exposed to high oxygen partial pressures have at the same time led to the discovery of ultrathin well-ordered films of oxides, so-called surface oxides on the surfaces of Ag, Rh, Pd, and Pt.^{9,15–21} A surface oxide can be viewed as an intermediate state in between the metallic phase and the formation of the bulk oxide. It is clear that the formation of a surface or a bulk oxide completely alters most properties of the originally metallic surface; thus, any information on the oxidation of transition-metal surfaces, and the resulting adsorption and reactivity properties, is valuable.^{11,22,23}

Most of these studies are, however, still limited to single-crystal low-index surfaces, a condition rarely found in nature, where surfaces normally contain a large number of defects and facets. In fact, a typical metallic particle, used in, for example, catalysis, is expected to oxidize more easily and to a larger extent than a single crystal, forming not only surface oxides resulting in a core-shell structure but also a more complete oxidation of the metal particle.^{24,25} It is, however, not straightforward to experimentally study metal particles on the atomic scale under realistic conditions, as the oxidation behavior can be surprisingly complex.²⁶

One way to increase the complexity of a surface on the route towards real metal particles is to use vicinal surfaces; see, for example, Refs. 27–30. Such a surface provides a large number of “defects,” which in some aspects have properties similar to those expected on metal particles. In particular, the atoms at a step edge of a vicinal surface have a

similar (under)coordination as atoms between different facets on a nanoparticle. Because of this undercoordination, atoms at step edges are expected to be more reactive in their interaction with the surrounding gas. We have recently shown that in the case of a Pt(332) surface, the dissociation and sticking probability of the O₂ molecule is enhanced as compared to the (111) surface, leading to the formation of a one-dimensional (1D) oxide along the step edge. It could also be shown that the 1D oxide is more reactive in the CO oxidation as compared to the chemisorbed oxygen on the Pt(111) terraces.³¹

In this study we show that a combination of experimental and theoretical methods is able to unravel the atomistic mechanisms governing oxygen-induced morphology changes of a vicinal Rh(553) surface. At intermediate oxygen partial pressures, this surface is rearranged into coexisting (331) and (111) facets. Along the steps on the (331) facets, a 1D nano-segmented oxide is formed, while the (111) facets are covered with oxygen in a (2 × 1) structure similar to that on the Rh(111) surface.^{32,33} At higher oxygen partial pressures the (331) facets disappear, and we find (111) facets only, covered by a two-dimensional O-Rh-O trilayer surface oxide.⁹ This demonstrates that large morphological changes, on mesoscopic as well as atomic length scales, can be induced by surprisingly low O partial pressures. In turn this implies that most of the important properties of a catalytic nanoparticle such as its shape, geometrical, and electronic structure may be completely transformed as the particle is exposed to an enhanced gas pressure and/or temperature. This result and its implications for other gas-surface combinations are highly relevant for understanding heterogeneous catalysis, as the detailed atomic geometry and composition of the catalyst surface under working conditions are necessary ingredients in such an understanding.^{27,34,35} It may also have significant consequences in several common uses of vicinal surfaces such as growth templates for various nanostructures³⁶ as well as for chiral biomolecules.³⁷

II. EXPERIMENT

The low-energy electron diffraction (LEED) and high-resolution core level spectroscopy (HRCLS) measurements were done using a sample temperature of 90 K at beamline I311 (Ref. 38) at MAX-lab, Lund, Sweden, using a normal emission angle and photon energies of 380 and 625 eV for the Rh 3d_{5/2} and O 1s levels, respectively.

Scanning tunneling microscopy (STM) images were recorded using a commercial Omicron STM1, operated at room temperature in Lund, Sweden. The STM is positioned inside an UHV system with a base pressure of 1 × 10⁻¹⁰ mbar. STM tips used in these experiments were all chemically etched tungsten tips. All images shown were recorded in constant current mode.

The surface x-ray diffraction (SXRD) measurements were carried out at the ID3 surface diffraction beamline³⁹ at the European Synchrotron Radiation Facility (ESRF) using a photon energy of 17 keV. The experimental end station used is specifically constructed for studies under high pressures and elevated sample temperatures.⁴⁰ The crystal basis used to

describe the (*HKL*) directions is a monoclinic basis set, which for the (553) coordinates give $\mathbf{a}_1=(a_0/2, a_0/2, 0)$, $\mathbf{a}_2=(-3/2a_0, 0, 5/2a_0)$, and $\mathbf{a}_3=(5a_0, -5a_0, 3a_0)$, expressed as a function of the cubic Rh lattice, with \mathbf{a}_1 and \mathbf{a}_2 lying in the surface plane and of length 2.687 Å and 11.079 Å and \mathbf{a}_3 out of plane with length 29.188 Å. In this basis $\alpha=\beta=90^\circ$ and $\gamma=111.333^\circ$ ($a_0=3.80$ Å is the bulk Rh lattice constant).

III. MODELING

The calculations were performed using the Vienna *ab initio* simulation package (VASP).^{41,42} The calculations are based on the projector augmented-wave (PAW) method^{43,44} and generalized gradient (GGA) corrections as proposed by Perdew *et al.*⁴⁵ For the plane-wave set a cutoff energy of 250 eV was used. The surface was modeled by a slab consisting of six layers in the (111) direction. The Brillouin-zone integration was performed using a (4 × 8 × 1) Monkhorst-Pack grid for Rh(553) and a (8 × 8 × 1) grid for Rh(331). For the (10 × 1) reconstructions the number of points was reduced accordingly.

For the determination of the phase diagram the Gibbs free surface energy per area was calculated as

$$\gamma = (G_{\text{slab}} - N_{\text{Rh}}\mu_{\text{Rh}} - N_{\text{O}}\mu_{\text{O}})/A, \quad (1)$$

where G_{slab} is the total energy of the slab, N_{Rh} and N_{O} are the number of Rh and O atoms in the slab, and μ_{O} and μ_{Rh} are the chemical potentials of O and Rh. Vibrational contributions are neglected, except for μ_{O} , for which we have used the partition function of the ideal gas. The value μ_{Rh} is set to the calculated energy of bulk fcc Rh. The 0 K value for O₂ is taken from our total energy calculations. In Fig. 8, below, $\mu_{\text{O}}=0$ corresponds to this 0 K limit. The STM simulation was performed using the Tersoff-Hamann approach.⁴⁶

IV. RESULTS AND DISCUSSION

A. Clean surface

Figure 1(a) shows a model of the pristine Rh(553) surface which consists of five-atom-wide terraces separated by monoatomic {111}-faceted steps approximately 10 Å apart. Scanning tunneling microscopy, Fig. 1(b), directly confirms the expected surface structure of the present sample displaying a distance of approximately 10–11 Å between steps. Additional LEED [Fig. 1(c)] and SXRD measurements shown in Fig. 1(d) confirmed the presence of a well-ordered Rh(553) surface. The intensity of the peaks at integer values of K is determined at which L value the bulk Bragg reflection occurs.

B. Faceting and formation of a 1D oxide

Exposing the surface to about 5 × 10⁻⁶ mbar of O₂ at 380 °C causes dramatic changes as displayed in the LEED image of Fig. 2(a). It is still rather straightforward to identify the (1 × 1) spots (large hexagon) and an oxygen-induced (2 × 1) superstructure (small hexagon) from the (111) facets; however, a change in the periodicity of the step-induced spots can be detected by measuring the distance between the

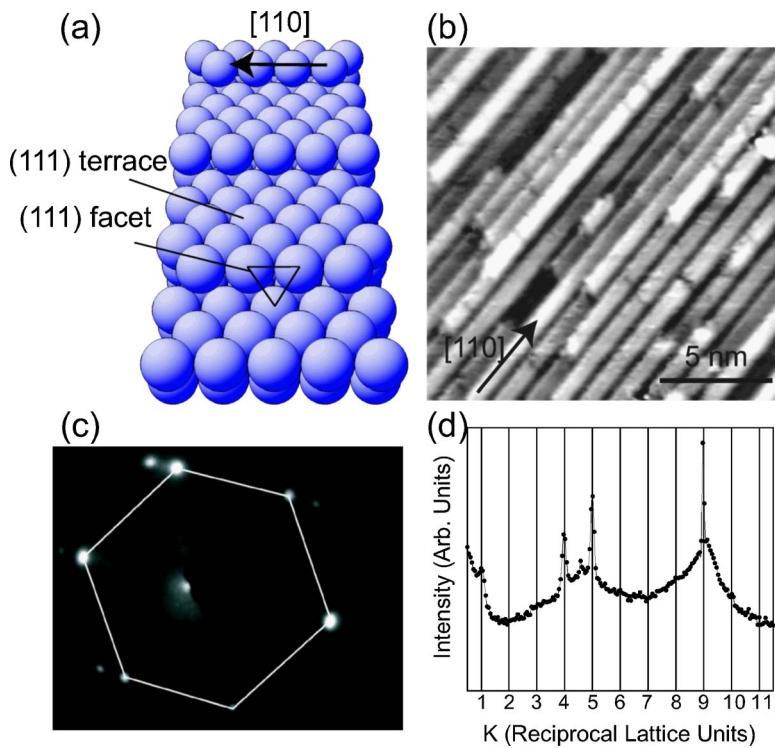


FIG. 1. (Color online) (a) Model of the Rh(553) surface. (b) STM image ($200 \times 200 \text{ \AA}^2$) of the clean Rh(553) surface, using a positive sample bias of 2.8 V and a tunneling current of 0.3 nA. (c) LEED pattern from the clean Rh(553). The diffraction spots from the (111) terraces are indicated. (d) SXR scan from the Rh(553) surface in the K direction with $H=0$ and $L=0.5$ plotted in (553) coordinates.

spots in the K direction. From the LEED pattern, we can conclude that the size of the terraces between the steps has decreased, indicating step bunching. Furthermore, additional spots can be seen, indicating that the surface is reconstructed along the steps, with a periodicity of around 10.

A more precise determination of the facets can be made by using SXR; see Figs. 2(b) and 2(c). Figure 2(b) shows K scans parallel to the (111) terraces at $H=0$ (no momentum transfer parallel to the steps) for different L values (momentum transfer normal to surface), plotted using Rh(553) coordinates. Apart from the $(0, -4, L)$ crystal truncation rod (CTR), additional rods, which are not constant in K with increasing L , are observed around $K=-2$ and as shoulders on both sides of the CTR at $K=-4$. This is direct proof for the formation of facets on the surface, since any facet will give rise to a CTR perpendicular to that facet.⁴⁷ Using instead (331) coordinates [Fig. 2(c)], two of the peaks stay constant at $K=-1$ and $K=-2$, respectively, unambiguously demonstrating the presence of (331) facets. In a similar way, the peak around $K=-4.3$ in the (553) coordinates is shown to correspond to (111) facets, which are also present on the clean (553) surface, but increase in strength as a result of the step bunching and faceting.

Direct confirmation by STM of these findings is shown in Fig. 3(a). This image shows an alternation between flat sur-

face areas and areas with a clearly discernable stepped structure. The stepped areas correspond to the (331) facets while the flat areas are (111) facets. On the flat areas, a (2×1) superstructure and characteristic rows of the (9×9) trilayer O-Rh-O surface oxide are seen. These observations confirm the above results obtained by diffraction methods; thus, the flat areas are (111) facets with O-induced (2×1) and (9×9) structures as expected on (111) terraces.^{9,32,33} Furthermore, a periodic structure is observed along the steps in the stepped areas of the (331) facets with a periodicity of around ten interatomic Rh distances, directly confirming the reconstruction along the steps as observed in LEED in Fig. 2(a).

Concentrating on the reconstruction along the steps as observed in the LEED pattern in Fig. 2(a), the STM image in Fig. 3(b) from a (331) facet reveals segmented chains, each containing eight protrusions. The protrusions are shifted by half a nearest-neighbor distance between two adjacent steps. Our model for the segmented chain, Fig. 3(d), is based on results of Africh *et al.*⁴⁸ for Rh(110)- (10×2) . Two out of ten Rh step-edge atoms are removed, leaving segments of eight Rh atoms, stretched out to cover nine original atomic distances, separated by one atomic distance. Furthermore, each step-edge Rh atom is surrounded by four O atoms. This, in combination with a change of the Rh-Rh distance to a value closer to bulk Rh_2O_3 , makes us refer to this as a one-

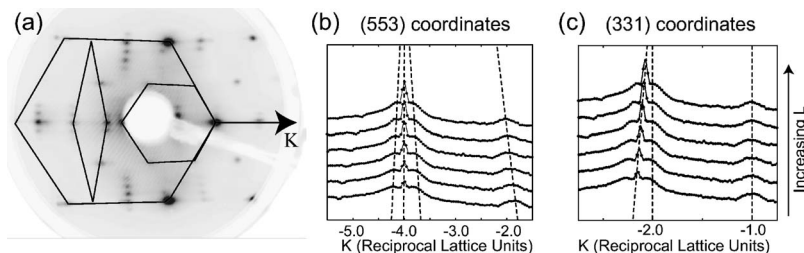


FIG. 2. (a) LEED image of the Rh(553) surface after an oxygen exposure of 5×10^{-6} mbar for 600 s at a sample temperature of 380 °C. The (1×1) (large hexagon) and (2×1) (small hexagon) from the (111) facets and the (1×1) from the oxygen-induced (331) facets are indicated. (b) and (c) SXR scans from the oxygen-exposed surface in the K direction with $H=0$ plotted in (553) and (331) coordinates, respectively.

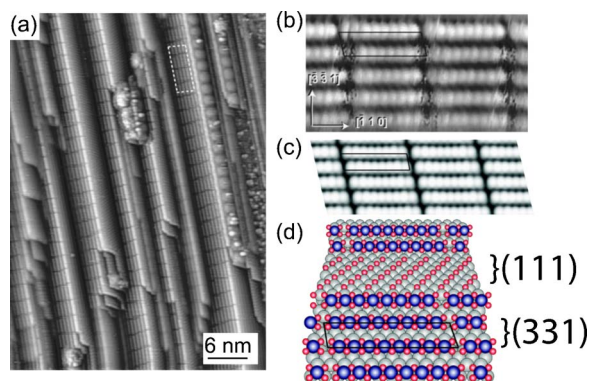


FIG. 3. (Color online) (a) STM image of the Rh(553) surface after an oxygen exposure of 5×10^{-6} mbar for 600 s at a sample temperature of 380 °C, using a negative sample bias of $V = -0.8$ V and a tunneling current of $I = 0.3$ nA. (b) Zoom-in STM image on a (331) facet (70×30 Å, $U = -0.8$ V, $I = 0.3$ nA). (c) Simulated STM image of the (331) facets decorated with oxygen atoms in a (10×1) pattern according to the model in d. (d) Model of the surface morphology and atomic arrangement (oxygen, red balls; Rh at the step edges, blue balls; Rh, gray balls). Note the one-dimensional oxide formed on the steps of the (331) surface.

dimensional oxide. The observed shift between chains on adjacent steps is not present on Rh(110)- (10×2) , but confirms the presence of (331) facets, since such a shift is intrinsic to this surface. Figure 3(c) shows the STM image as simulated by density functional theory⁴⁶ (DFT) according to the model presented in Fig. 3(d) and further discussed below. Here, the gap shift between adjacent steps is, for simplicity, chosen to be in the same direction all the time, while in the experimental data, the shift direction is varying, forming a zigzag pattern. Our DFT calculations do not show any energy difference between these two cases. Except for this difference, the similarity between theory and experiment is good, strongly supporting the model in Fig. 3(d).

Figure 4 shows the HRCLS results from the (331)-faceted surface. The O 1s spectrum reveals a single component at a binding energy of 529.7 eV, while the Rh $3d_{5/2}$ spectrum is decomposed into four different components. Starting with the O 1s component, the single peak can be explained by all O atoms being coordinated to three Rh atoms according to our model. The Rh $3d_{5/2}$ spectrum is more complex. As mentioned above, on the (111) terraces we have a (2×1) structure which has been described for the Rh(111) surface, together with the corresponding core-level shifts, by Ganduglia-Pirovano *et al.*³² This structure has two kinds of Rh atoms, coordinated to one and two oxygen atoms, respectively, giving rise to the peaks denoted 1O and 2O in Fig. 4. The remaining component can therefore be assigned to the Rh atoms at the step edges, which are all coordinated to four O atoms shifting the component towards higher binding energy. In passing we note that a simple additive model⁴⁹ would result in a shift between the 2O and 4O components twice as large as that observed. A similar effect of a smaller than expected shift of the metal core levels was also observed³¹ for the case of the one-dimensional oxide on Pt(332). These details regarding the magnitude of the core level shifts of the 1D oxide will be discussed together with

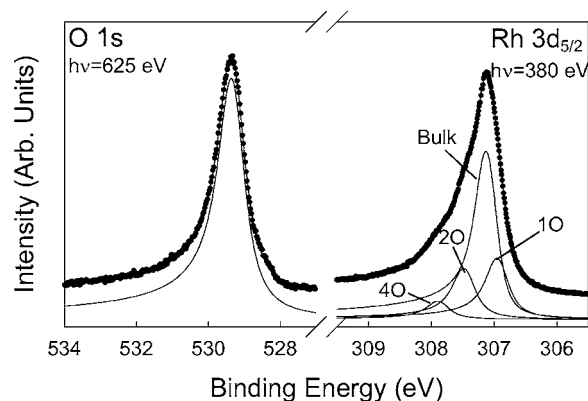


FIG. 4. HRCLS spectra from the Rh(553) surface after an oxygen exposure of 5×10^{-6} mbar for 600 s at a sample temperature of 380 °C. The Rh $3d_{5/2}$ spectra can be decomposed into components corresponding to onefold, twofold, and fourfold oxygen-coordinated Rh atoms, while the O 1s consists of one component.

changes in the electronic structure along the 1D nano-oxide chain in a separate article.⁵⁰ In summary, the HRCLS measurements confirm the model presented in Fig. 3(d).

C. Formation of (111) and $(11\bar{1})$ facets

Exposing the Rh(553) surface to an O₂ pressure of 10^{-3} mbar at a temperature of 550 °C results in a LEED pattern very similar to that of the (9×9) surface oxide structure previously found on Rh(111) (Ref. 9); see Fig. 5(a). The fact that we see the (9×9) coincidence also in the direction perpendicular to the steps indicates that the (111) facets are more than nine atoms wide. Figures 5(b) and 5(c) show SXRD scans parallel to the (111) surface at $H=0$ and different L values plotted using the (553) and (111) coordinates, respectively. At these O partial pressures, the (331) CTR's have disappeared and the (111) CTR has increased in intensity, indicating larger and more well-ordered (111) terraces. This result demonstrates that the steps merge to form Rh(111) and equivalent $(11\bar{1})$ facets [compare Fig. 6(b)]. Furthermore, we also find a new peak at $K = -0.89$ r.l.u. (where r.l.u. stands for reciprocal lattice units) in the (111) frame. This is exactly the value found for the surface oxide on Rh(111),⁹ confirming the formation of the (9×9) surface oxide on the (111)-faceted surface.

The high-resolution core-level spectroscopy results (Fig. 6) also show good agreement with those recorded for the Rh(111)- (9×9) ,⁸ strongly indicating the presence of the trilayer O-Rh-O surface oxide. The deconvolution process and origin for each component in Fig. 6(a) are described in detail in Ref. 8. The interface and surface components in the O 1s refer to the two types of oxygens in the O-Rh-O surface oxide, while the oxide and interface components in the Rh $3d_{5/2}$ spectrum refer to Rh in the O-Rh-O surface oxide at the interface in between the surface oxide and the bulk Rh. The experimental results shown in Figs. 5 and 6 lead us to the model shown in Fig. 6(b): the step bunching has now proceeded as far as possible, with only (111) and $(11\bar{1})$ facets

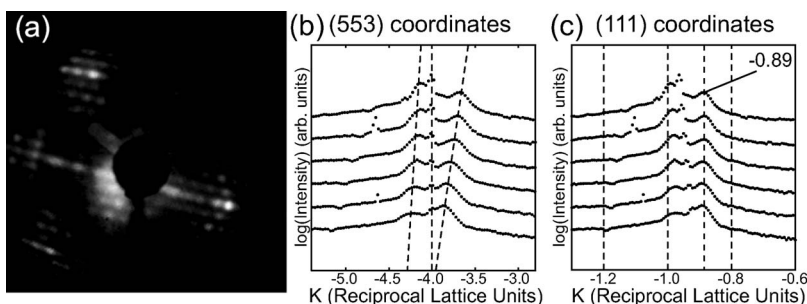


FIG. 5. (a) LEED image of the Rh(553) surface after an oxygen exposure of 5×10^{-3} mbar for 600 s at a sample temperature of 550 °C. The diffraction spots from the (9×9) structure on the (111) facets strongly indicate increased step bunching. (b) and (c) SXR scans from the oxygen-exposed surface in the K direction with $H=0$ plotted in (553) and (111) coordinates, respectively. The peak at $K=-0.89$ in (c) shows the presence of the (9×9) surface oxide found on Rh(111) (Ref. 9) on the (111) facets.

remaining. These facets are covered by the trilayer surface oxide.

D. Theoretical insights

To gain insight into the details of the driving force for the oxygen-induced faceting and successive merging of the steps, we turn to *ab initio* DFT calculations. As well for Rh(553) as for Rh(331) the stable oxygen structures have been determined by comparing several adsorption configurations for an successively increased oxygen coverage. The energetically most stable structures have been used to construct a phase diagram as described in Sec. III. Thus, we have calculated a comprehensive surface phase diagram considering Rh(553), a reconstruction of the Rh(553) surface into Rh(331) and Rh(111) facets, and finally into facets

showing exclusively Rh(111) and Rh(111̄) orientation [Fig. 7(a)].

In the low-coverage limit on Rh(553) the oxygen atoms are predicted to adsorb in hollow sites located above the step edge [Fig. 7(b)]. Due to the influence of the step, the DFT adsorption energy of 2.20 eV is slightly larger than the calculated value for the clean (111) surface, 2.05–2.11 eV.³³ Adsorption at the lower step edge is found to be rather unfavorable (1.78 eV).

With increasing oxygen coverage the terrace is successively filled via a local $p(2 \times 2)$ structure until the adsorbate-adsorbate repulsion on the terraces is high enough for occupation of the lower steps to become favorable, leading to a coexistence of a $p2mg$ -like zigzag structure on the steps and a $p(2 \times 1)$ structure on the terraces [Fig. 7(c)]. If the oxygen coverage is increased further, the above-mentioned (10×1) phase is formed at the step edge and the terraces remain covered by a local (2×1) phase [Fig. 7(d)].

Oxygen adsorption on the (331) surface proceeds in a similar manner. At low coverages, the oxygen atoms adsorb

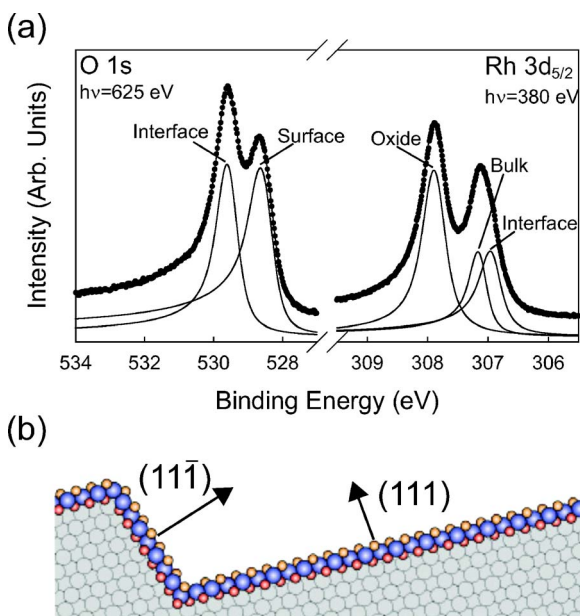


FIG. 6. (Color online) (a) HRCL spectra from the Rh(553) surface after an oxygen exposure of 5×10^{-3} mbar for 600 s at a sample temperature of 500 °C. The spectra strongly indicate the presence of the (9×9) structure on the (111) facets. (b) Model of the completely (111)- and $(111\bar{1})$ -faceted Rh(553) surfaces with the surface oxide structure on the surface.

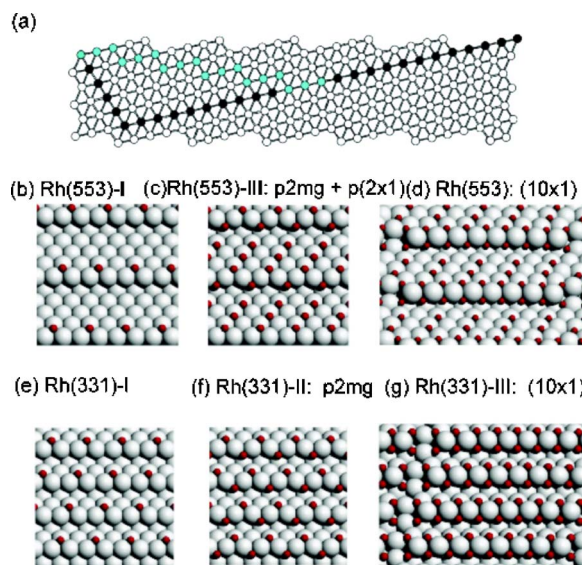


FIG. 7. (Color online) (a) Faceting of Rh(553) into Rh(331) (blue/grey atoms) and Rh(111) (black atoms), (b)–(d) calculated adsorption structures for O on Rh(553), and (e)–(g) O on Rh(331).

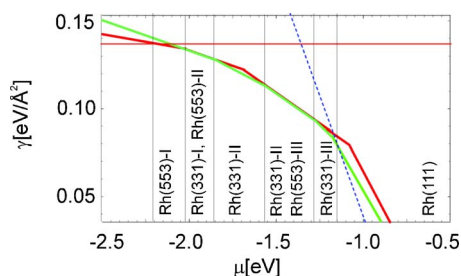


FIG. 8. (Color online) Phase diagram comparing O/Rh(553) to O/Rh(331)+O/Rh(111): dark gray (red) (553) phases, light gray (green) (331) phases, and dashed (blue) (111) surface oxide.

at the step edge with an adsorption energy of 2.18 eV [Fig. 7(e)], followed by a $p2mg$ -like decoration of the steps [Fig. 7(f)] and finally the same (10×1) reconstruction with two out of ten Rh step atoms missing [Fig. 7(g)]. The important point here is that this phase is significantly more stable on Rh(331) than on Rh(553). On Rh(553), the one-dimensional surface oxide at the steps coexists with a $p(2 \times 1)$ structure on the terraces. The simultaneous existence of the $p(2 \times 1)$ structure on the terraces and the 1D oxide at the steps leads to a high local O concentration in the vicinity of the steps; see Fig. 7(d). On Rh(331), however, the step edges are exclusively covered, because the terraces are too narrow to accommodate additional oxygen. The effective surface coverage for the Rh(331)- (10×1) is nevertheless larger than for the Rh(553)- (10×1) (0.107 oxygen/ \AA^2 compared to 0.094). The driving force for the step bunching is the unfavorable interface between the $p(2 \times 1)$ -O structure on the terrace and the one-dimensional surface oxide at the edges. When the terrace areas of the (553) surface “bunch” together to form large continuous (111) areas with a local $p(2 \times 1)$ -O adatom structure, interfaces between the $p(2 \times 1)$ -O and the reconstructed step edge are minimized, as illustrated in Fig. 7(a); originally each (553) unit cell exhibits an interface, while after the step bunching the stepped (331) and the flat (111) areas are separated.

Figure 8 shows the phase diagram comparing the Gibbs free surface energy of oxygen adsorbed on Rh(553) to a combination of Rh(331) and Rh(111) areas, yielding the same average macroscopic crystallographic orientation. The Gibbs free energies of the Rh(553) and the Rh(331)+Rh(111) surfaces are almost degenerate for most coverages with equivalent structures on both surfaces. However, a large driving force towards Rh(331) is observed around a chemical potential of $\mu = -1.1$ eV, its origin being the unfavorable interface. In fact the experimental conditions (5×10^{-6} mbar, 380 °C) correspond to a chemical potential of $\mu = -1.18$ eV, close to our calculated value.

When the chemical potential is increased even further, the whole surface is predicted to reconstruct into Rh(111) sur-

face areas covered with the (9×9) surface oxide as this allows for the highest oxygen content per area. In this case, the increase in effective surface area [compare Fig. 7(a)] is more than made up for by the increased stability of the surface oxide on Rh(111). Although we find that step bunching is thermodynamically favorable in a small regime before the onset of the surface oxide, a large driving force exists only for chemical potentials at which the surface-oxide covered (111) facets are already stable.

V. CONCLUSION

The results presented above demonstrate that the initial oxidation of Rh(553) on the atomic scale involves step bunching, rearranging the surface into lower-index facets. Increasing the oxygen partial pressure sufficiently, the Rh(553) surface becomes unstable towards a separation into (331) and (111) facets coexisting on the surface. As well for the (10×1) one-dimensional oxide structure on the (331) facets as for the (2×1) structure on the (111) facets the experimental data agree perfectly with the theoretical predictions. In the first stage, this leads to (331) and (111) facets coexisting on the surface, where the (331) facets show a (10×1) one-dimensional oxide structure, while the (111) facets display a (2×1) structure. At higher O_2 exposures the surface is completely rearranged into $\{111\}$ facets covered by the (9×9) surface oxide, allowing for the highest oxygen content per area. Again, for these observations the experimental and theoretical results show remarkable agreement. The study demonstrates how a combination of several experimental techniques and state-of-the-art DFT calculations can lead to a detailed understanding of complex gas-induced surface rearrangements also on more mesoscopic length scales. The results show that the precise matching of the terrace and step structures is of key importance for the understanding of the physics of rough surfaces. They also indicate that the defect structure of a nanoparticle used, e.g., for catalysis as well as vicinal template surfaces used for the study of nanostructures and chiral biomolecules may be significantly rearranged in the presence of surprisingly low amounts of oxygen.

ACKNOWLEDGMENTS

This work was financially supported by the Swedish Research Council, the Crafoord Foundation, the Knut and Alice Wallenberg Foundation, the Austrian *Fonds zur Förderung der wissenschaftlichen Forschung*, the MCyT of the Spanish Government (Project No. MAT2002-02808), and the European Union under Contract No. NMP3-CT-2003-505670 (NANO2). Support by the MAX-lab and ESRF staff is gratefully acknowledged.

*Electronic address: Edvin.Lundgren@sljus.lu.se

- ¹Frontiers in Surface and Interface Science, edited by C. B. Duke and E. W. Plummer [Surf. Sci. **500**, 1 (2001)].
- ²G. Ertl, H. Knözinger, and J. Weitkamp, *Handbook of Heterogeneous Catalysis* (Wiley, New York, 1997).
- ³K. F. Peters, C. J. Walker, P. Steadman, O. Robach, H. Isern, and S. Ferrer, Phys. Rev. Lett. **86**, 5325 (2001).
- ⁴L. Österlund, P. B. Rasmussen, P. Thostrup, E. Lægsgaard, I. Stensgaard, and F. Besenbacher, Phys. Rev. Lett. **86**, 460 (2001).
- ⁵E. K. Vestergaard, R. T. Vang, J. Knudsen, T. M. Pedersen, T. An, E. Lægsgaard, I. Stensgaard, B. Hammer, and F. Besenbacher, Phys. Rev. Lett. **95**, 126101 (2005).
- ⁶B. L. M. Hendriksen and J. W. M. Frenken, Phys. Rev. Lett. **89**, 046101 (2002).
- ⁷B. L. M. Hendriksen and J. W. M. Frenken, Surf. Sci. **552**, 229 (2004).
- ⁸J. Gustafson, A. Mikkelsen, M. Borg, E. Lundgren, L. Köhler, G. Kresse, M. Schmid, P. Varga, J. Yuhara, X. Torrelles, C. Quirós, and J. N. Andersen, Phys. Rev. Lett. **92**, 126102 (2004).
- ⁹E. Lundgren, J. Gustafson, A. Mikkelsen, J. N. Andersen, A. Stierle, H. Dosch, M. Todorova, J. Rogal, K. Reuter, and M. Scheffler, Phys. Rev. Lett. **92**, 046101 (2004).
- ¹⁰Y. B. He, M. Knapp, E. Lundgren, and H. Over, J. Phys. Chem. B **109**, 21825 (2005).
- ¹¹M. D. Ackermann, T. M. Pedersen, B. L. M. Hendriksen, O. Robach, S. C. Bobaru, I. Popa, C. Quiros, H. Kim, B. Hammer, S. Ferrer, and J. W. M. Frenken, Phys. Rev. Lett. **95**, 255505 (2005).
- ¹²A. Stierle, N. Kasper, H. Dosch, J. Gustafson, A. Mikkelsen, J. N. Andersen, and E. Lundgren, J. Chem. Phys. **122**, 44706 (2005).
- ¹³G. Ketteler, D. F. Ogletree, H. Bluhm, H. J. Liu, E. L. D. Hebenstreit, and M. Salmeron, J. Am. Chem. Soc. **127**, 18269 (2005).
- ¹⁴H. Over, Y. D. Kim, A. P. Seitsonen, S. Wendt, E. Lundgren, M. Schmid, P. Varga, A. Morgante, and G. Ertl, Science **287**, 1474 (2000).
- ¹⁵C. I. Carlisle, D. A. King, M.-L. Bocquet, J. Cerdá, and P. Sautet, Phys. Rev. Lett. **84**, 3899 (2000).
- ¹⁶M. Schmid, A. Reicho, A. Stierle, I. Costina, J. Klikovits, P. Kostelnik, O. Dubay, G. Kresse, J. Gustafson, E. Lundgren, J. N. Andersen, H. Dosch, and P. Varga, Phys. Rev. Lett. **96**, 146102 (2006).
- ¹⁷J. Schnadt, A. Michaelides, J. Knudsen, R. T. Vang, K. Reuter, E. Lægsgaard, M. Scheffler, and F. Besenbacher, Phys. Rev. Lett. **96**, 146101 (2006).
- ¹⁸E. Lundgren, G. Kresse, C. Klein, M. Borg, J. N. Andersen, M. De Santis, Y. Gauthier, C. Konvicka, M. Schmid, and P. Varga, Phys. Rev. Lett. **88**, 246103 (2002).
- ¹⁹M. Todorova, E. Lundgren, V. Blum, A. Mikkelsen, S. Gray, J. Gustafson, M. Borg, J. Rogal, K. Reuter, J. N. Andersen, and M. Scheffler, Surf. Sci. **541**, 101 (2003).
- ²⁰W. X. Li, L. Österlund, E. K. Vestergaard, R. T. Vang, J. Matthiesen, T. M. Pedersen, E. Lægsgaard, B. Hammer, and F. Besenbacher, Phys. Rev. Lett. **93**, 146104 (2004).
- ²¹J. Gustafson, A. Mikkelsen, M. Borg, J. N. Andersen, E. Lundgren, C. Klein, W. Hofer, M. Schmid, P. Varga, L. Köhler, G. Kresse, N. Kasper, A. Stierle, and H. Dosch, Phys. Rev. B **71**, 115442 (2005).
- ²²H. Over, A. P. Seitsonen, E. Lundgren, M. Schmid, and P. Varga, J. Am. Chem. Soc. **123**, 11807 (2001).
- ²³E. Lundgren, J. Gustafson, A. Resta, J. Weissenrieder, A. Mikkelsen, J. N. Andersen, L. Köhler, G. Kresse, J. Klikovits, A. Biederman, M. Schmid, and P. Varga, J. Electron Spectrosc. Relat. Phenom. **144**, 367 (2005).
- ²⁴G. Rupprechter, K. Hayek, and H. Hofmeister, J. Catal. **173**, 409 (1998).
- ²⁵J. Assmann, D. Crihan, M. Knapp, E. Lundgren, E. Löffler, M. Muhler, V. Narkhede, H. Over, M. Schmid, A. Seitsonen, and P. Varga, Angew. Chem., Int. Ed. **44**, 917 (2005).
- ²⁶T. Schalow, M. Laurin, B. Brandt, S. Schaueremann, S. Guimond, H. Kühlenbeck, D. E. Starr, S. K. Shaikhutdinov, J. Libuda, and H. J. Freund, Angew. Chem., Int. Ed. **44**, 7601 (2005).
- ²⁷B. Lang, R. W. Joyner, and G. A. Somorjai, Surf. Sci. **30**, 454 (1972).
- ²⁸D. G. Castner and G. A. Somorjai, Surf. Sci. **83**, 60 (1979).
- ²⁹G. A. Somorjai, *Chemistry in Two Dimensions: Surfaces* (Cornell University Press, London, 1981).
- ³⁰D. Hoogers and D. A. King, Surf. Sci. **286**, 306 (1993).
- ³¹J. G. Wang, W. X. Li, M. Borg, J. Gustafson, A. Mikkelsen, T. M. Pedersen, E. Lundgren, J. Weissenrieder, J. Klikovits, M. Schmid, B. Hammer, and J. N. Andersen, Phys. Rev. Lett. **95**, 256102 (2005).
- ³²M. V. Ganduglia-Pirovano, M. Scheffler, A. Baraldi, S. Lizzit, G. Comelli, G. Paolucci, and R. Rosei, Phys. Rev. B **63**, 205415 (2001).
- ³³L. Köhler, G. Kresse, M. Schmid, E. Lundgren, J. Gustafson, A. Mikkelsen, M. Borg, J. Yuhara, J. N. Andersen, M. Marsman, and P. Varga, Phys. Rev. Lett. **93**, 266103 (2004).
- ³⁴K. Honkala, A. Hellman, I. N. Remediakis, A. Logadottir, A. Carlsson, S. Dahl, C. H. Christensen, and J. K. Nørskov, Science **307**, 555 (2005).
- ³⁵R. T. Vang, K. Honkala, S. Dahl, E. K. Vestergaard, J. Schnadt, E. Lægsgaard, B. S. Clausen, J. K. Nørskov, and F. Besenbacher, Nat. Mater. **4**, 160 (2005).
- ³⁶P. Gambardella, A. Dallmeyer, K. Maiti, M. C. Malagoli, W. Eberhardt, K. Kern, and C. Carbone, Nature (London) **416**, 301 (2002).
- ³⁷A. Ahmadi, G. Attard, J. Feliu, and A. Redes, Langmuir **15**, 2420 (1999).
- ³⁸R. Nyholm *et al.*, Nucl. Instrum. Methods Phys. Res. A **467-468**, 520 (2001).
- ³⁹S. Ferrer and F. Comin, Rev. Sci. Instrum. **66**, 1674 (1995).
- ⁴⁰P. Bernard, K. Peters, J. Alvarez, and S. Ferrer, Rev. Sci. Instrum. **70**, 1478 (1999).
- ⁴¹G. Kresse and J. Hafner, Phys. Rev. B **47**, 558 (1993).
- ⁴²G. Kresse and J. Furthmüller, Comput. Mater. Sci. **6**, 15 (1996).
- ⁴³P. E. Blöchl, Phys. Rev. B **50**, 17953 (1994).
- ⁴⁴G. Kresse and D. Joubert, Phys. Rev. B **59**, 1758 (1999).
- ⁴⁵J. P. Perdew, J. A. Chevary, S. H. Vosko, K. A. Jackson, M. R. Pederson, D. J. Singh, and C. Fiolhais, Phys. Rev. B **46**, 6671 (1992).
- ⁴⁶J. Tersoff and D. R. Hamann, Phys. Rev. B **31**, 805 (1985).
- ⁴⁷D. A. Walko and I. K. Robinson, Phys. Rev. B **59**, 15446 (1999).
- ⁴⁸C. Africh, F. Esch, W. X. Li, M. Corso, B. Hammer, R. Rosei, and G. Comelli, Phys. Rev. Lett. **93**, 126104 (2004).
- ⁴⁹A. Nilsson, B. Eriksson, N. Mårtensson, J. N. Andersen, and J. Onsgaard, Phys. Rev. B **38**, 10357 (1988).
- ⁵⁰F. Mittendorfer, G. Kresse, J. Gustafson, J. N. Andersen, and E. Lundgren (unpublished).